Materials design and development of functional materials for industry

2008 J. Phys.: Condens. Matter 20 064227

(http://iopscience.iop.org/0953-8984/20/6/064227)

IOP PUBLISHING JOURNAL OF PHYSICS: CONDENSED MATTER

J. Phys.: Condens. Matter **20** (2008) 064227 (7pp) doi:10.1088/0953-8984/20/6/064227

Materials design and development of functional materials for industry

Ryoji Asahi[1], **Takeshi Morikawa, Hirofumi Hazama and Masato Matsubara**

Toyota Central R&D Laboratories Incorporated, Nagakute, Aichi 480-1192, Japan

E-mail: rasahi@mosk.tytlabs.co.jp

Received 7 September 2007
Published 24 January 2008
Online at stacks.iop.org/JPhysCM/20/064227

Abstract

It is now well recognized that we are witnessing a golden age of innovation with novel materials, with discoveries that are important for both basic science and industry. With the development of theory along with computing power, quantum materials design—the synthesis of materials with the desired properties in a controlled way via materials engineering on the atomic scale—is becoming a major component of materials research. Computational prediction based on first-principles calculations has helped to find an efficient way to develop materials that are much needed for industry, as we have seen in the successful development of visible-light sensitized photocatalysts and thermoelectric materials. Close collaboration between theory and experiment is emphasized as an essential for success.

1. Introduction

The load placed on our environment has grown tremendously in recent years because of increased consumption of resources and energy, fueled by entrenched socio-economic activities based on mass production, mass consumption, and mass waste. Under such circumstances, we have to make continuous efforts to develop new materials that tackle global environmental issues such as environmental decontamination, CO_2 reduction, and sustainable resource and energy supply, which are also of great concern for the entering into force of the Kyoto Protocol.

With the development of theory along with computing power, quantum materials design—the synthesis of materials with the desired properties in a controlled way via materials engineering on the atomic scale—is becoming a major component of materials research. Computational prediction based on first-principles calculations has successfully helped to find an efficient way to develop materials, as demonstrated recently in visible-light photocatalysts [1], high-performance thermoelectric materials [2, 3], and super elasto-plastic titanium alloys [4]. In these examples, we have seen that first-principles calculations and experiments work together indeed improve the materials properties to reach a realistic production level.

In this paper, general aspects of computational materials design by using first-principles calculations are first described. Since a comprehensive review of the recent progress in first-principles calculations has been reported recently [5], here we emphasize points that are particularly important for materials design in industrial applications. We then present the recent development of photocatalysts and thermoelectric materials, enlightening how computational materials design plays an important role in collaboration with experimental works.

2. General strategies of the materials design

We typically employ the following steps for materials design in industry:

(1) Set target properties required for materials.
(2) Choose a benchmark system.
(3) Construct a computational model.
(4) Compute the bench mark system.
(5) Predict a new system.

In step (1), we usually set the target properties so that they can satisfy the industrial or social requirements. No materials structure is assumed in this stage. However, prerequisites (or restrictions) for the constitution of materials are often enforced, namely to be environmentally benign and sustainable. The materials price is also to be considered as well. In step (2), we can take a material that shows the best performance so far reported for the target properties as an instructive benchmark. For this purpose, we can choose the material which does not

[1] Author to whom any correspondence should be addressed.

satisfy the above prerequisites. In step (3), since the real material system is often too complicated to simulate directly, one may construct a simple model capable of computations in a reasonable time but keeping the physical essence. This procedure requires considerable insight into the materials science, computational physics, and engineering aspects of the problem, and therefore close discussion with experimentalists is indispensable. In practice, one of the crucial discussions often made in industry is to judge the efficiency and meaning of the computation compared to experiment. However, one should keep in mind that the computation can access an extreme condition, such as the absence of impurities or very high pressure, which is not easily prepared in experiment, and may show the possible maximum properties of materials.

Computing the benchmark system in step (4), we carefully make sure of the computational accuracy and validity of the model by comparing with available experimental results. Without this knowledge, the consequences that are deduced can be wrong. The most important and powerful aspect of the computation is to understand the microscopic mechanism and to derive a materials trend for the target properties. This is followed by the prediction of a new system that may improve the target properties over the conventional benchmark systems, as in step (5). To this end, systematic modifications of the material by elementary substitution or doping can often be used. We can check the stability and/or process conditions to synthesize the candidates, which can convince people to do the experiment.

If we know a suitable benchmark system in advance, we can find some of the candidates smoothly from the above procedure. If not, however, one must introduce a new concept and choose a system which may or may not realize the target properties. Usually this is quite a difficult issue.

3. Visible-light sensitized photocatalysts

Since the photo-induced decomposition of water on TiO_2 electrodes was discovered [6], semiconductor-based photocatalysis has attracted extensive interest [7]. Most of the investigations, as well as the development of applications, have been focused on TiO_2, which shows relatively high reactivity and chemical stability under ultraviolet (UV) light (wavelengths $\lambda < 387$ nm) whose energy exceeds the band gap of 3.2 eV in the anatase crystalline phase. On the other hand, photocatalysts that can yield high reactivity under visible light ($\lambda > 380$ nm) are desired, as they should allow the main part of the solar spectrum and even poor illumination of interior lighting to be utilized. To this end, the following two ways of modifying TiO_2 have mainly been employed; one is to dope transition metals into TiO_2 [8–10], and another is to form reduced TiO_x photocatalysts [11, 12]. Both approaches introduce impurity/defect states in the band gap of TiO_2, which lead TiO_2 to absorb visible light. However, subtle issues reside in the nature of these impurity states. First, reducing TiO_2 introduces localized oxygen vacancy states located at 0.75–1.18 eV below the conduction band minimum (CBM) of TiO_2 [12], which may sacrifice the photo-reduction activity because a redox potential of the hydrogen evolution (H_2/H_2O) is located just below the CBM of TiO_2 [13]. Second, the transition metal doping, where quite localized d states appear deep in the band gap of the host semiconductor, often results in an increase in carrier recombination [9]. The probability of recombination increases with the concentration of trapping sites that capture an electron from the conduction band or a hole from the valence band, as described by the Shockley–Read–Hall model [14]. Therefore, if doping produces localized deep levels (E_i much larger than the thermal excitation energy k_BT) in the band gap, the lifetime of the mobile carriers may become shorter, giving low photocatalytic activity, as is typically observed in a system with transition metal doping.

We started by considering whether visible-light activity could be introduced in TiO_2 by doping, and we set the following requirements: (i) doping should produce states in the band gap of TiO_2 that absorb visible light; (ii) the CBM, including subsequent impurity states, should be as high as that of TiO_2 or higher than the H_2/H_2O level to ensure photoreduction activity; and (iii) the states in the gap should overlap sufficiently with the band states of TiO_2 to transfer photoexcited carriers to reactive sites at the catalyst surface within their lifetime. Conditions (ii) and (iii) resulted in the idea that anionic species can be suitable dopants for visible-light sensitization rather than cationic metals.

We calculated the densities of states (DOS) of the substitutional doping of C, N, F, P, or S for O in the anatase TiO_2 crystal by using the full-potential linearized augmented plane wave (FLAPW) formalism [15, 16] in the framework of the local density approximation (LDA) [17] as shown in figure 1(a). The substitutional doping of N was the most effective because its p states contribute to band-gap narrowing by mixing with O 2p. Although doping with S shows a similar band-gap narrowing, it would be difficult to incorporate it into the TiO_2 crystal because of its large ionic radius, as evidenced by a much larger formation energy required for the substitution of S than that required for the substitution of N. The states introduced by C and P are too deep in the gap to satisfy the above condition (iii). The calculated imaginary parts of the dielectric functions of $TiO_{2-x}N_x$ indeed show a shift of the absorption edge to a lower energy by N doping (figure 1(b)). Dominant transitions at the absorption edge have been identified with those from N $2p_\pi$ to Ti d_{xy}, instead of from O $2p_\pi$ as in TiO_2 [18].

The effectiveness of substitutional N doping was verified by experiment. Film samples prepared by sputtering the TiO_2 target in an N_2 (40%)/Ar gas mixture with post-annealing at 550 °C in N_2 gas, and powder samples prepared by treating anatase TiO_2 powder in an NH_3 (67%)/Ar atmosphere at 600 °C, showed significant photocatalytic activity under visible light, while both revealed similar activity to TiO_2 under UV light, as shown in figure 2. In fact, optical absorption spectra show that the $TiO_{2-x}N_x$ films noticeably absorb the light at less than 500 nm, whereas the TiO_2 films do not, which is in good agreement with the theoretical results. N 1s core levels were investigated by x-ray photoemission spectroscopy (XPS). The N-doped samples showed that the peak intensity at the binding energy of 396 eV, assigned to substitutional N for the O site, was well correlated with the photocatalytic activity. Thus

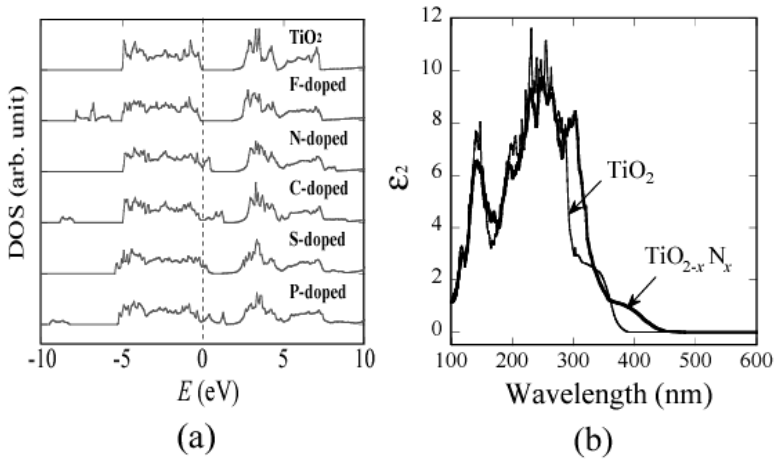

Figure 1. (a) Calculated total DOSs of doped TiO_2. The dopants F, N, C, S, and P were located at a substitutional site for an O atom in the anatase TiO_2 crystal (eight TiO_2 units per cell). The energy is measured from the top of the valence bands of TiO_2, and the DOS for doped TiO_2 is shifted so that the peaks of the O 2s states (at the furthest site from the dopant) are aligned with each other. (b) Calculated imaginary parts of the dielectric functions (ε_2), which are averaged over three (x, y, and z) polarization vectors, of $TiO_{2-x}N_x$ (thick lines) compared with TiO_2 (thin lines).

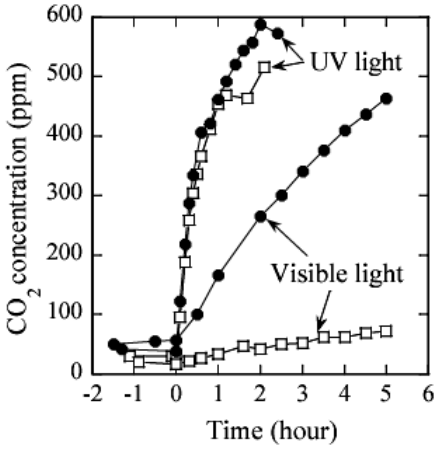

Figure 2. Photocatalytic properties of $TiO_{2-x}N_x$ samples (solid circles) compared with TiO_2 samples (open squares). CO_2 evolution as a function of irradiation time (light-on at zero) during the photodegradation of acetaldehyde gas (with an initial concentration of 485 parts per million (ppm)) under UV irradiation (BL with a peak at 351 nm and the light power of 5.4 mW cm^{-2}) and visible irradiation (fluorescent light cut by the optical high-path filter (SC42, Fuji Photo Film), with a peak intensity at 436 nm and a light power of 0.9 mW cm^{-2}).

the active site of N for photocatalysis under visible light was concluded to be the substitutional site.

Since the report of Asahi *et al* [1], a large number of studies have reported on the photocatalytic properties of N-doped TiO_2 under visible light, showing a promising extension of applications where the conventional TiO_2 is not used. However, arguments for the chemical nature of N and the mechanism of the visible-light response have not been reconciled to date. The hydrolysis of $TiCl_4$ with NH_4OH followed by calcination at 400 °C also lead to the formation of yellowish TiO_2 powder showing visible-light absorption [19]. Such an N species was assigned to be NO_x-type complex, which was consistent with the results of electron paramagnetic resonance (EPR) measurement on TiO_2 samples treated with ammonia and calcined at high temperature [20]. Chen and Burda suggested that the NO_x-type complex species with a binding energy of 400 eV is responsible for the visible light sensitization [21]. These experimental results suggest that the detailed N states in TiO_2 would vary with the employment of a nitrification process, and the assignment of their binding energies remains unsolved.

Considering a variety of nitrification processes, we introduced several kinds of N complex species including N, NO, and NO_2 into a substitutional site for O (denoted as $(NO)_O$ etc) or an interstitial site (denoted as $(NO)_i$ etc) in the anatase TiO_2 crystal. Note that the N_2 complex may be controlled by kinetics rather than thermodynamics, because two N atoms from different source points must arrive simultaneously at the same site, and thus formation can be suppressed when the N concentration is as small as that observed in experiment [22]. A supercell of 16 TiO_2 units (i.e. 48 atoms of the TiO_2 anatase matrix) was employed to simulate each kind of dopant, which is thus typically 3.1% N for O. We obtained the stable geometry by performing first-principles calculations using the projector augmented wave method [23] implemented in the Vienna *ab initio* simulation package (PAW-VASP) code [24, 25]. The generalized gradient approximation [26] was used as the exchange and correlation potential. To calculate band structures, we employed the FLAPW metho,d which treats all electrons, including the core electrons, self-consistently and relativistically, thus it is most suitable for comparing with the experimental XPS results. Note that an absolute value of the binding energy (a core level with respect to the Fermi energy) is not accurately evaluated from an eigenvalue of the single electron within the present theoretical framework. Instead, we calculated an energy difference (Δ_{N-Ti}) between the N 1s core level and an averaged value of Ti $2p_{3/2}$ over the unit cell. We then obtained the binding energy, $BE = \Delta_{N-Ti} + \Delta_0$, where a rigid offset Δ_0 is rather arbitrary, but here we set it

Table 1. Calculated N 1s binding energies, BE in eV, and their errors in eV estimated by the Ti $2p_{3/2}$ levels within the unit cell. The BE for $(N)_O$ is assumed to be an experimental value [27].

Dopant	BE	Error
$(N)_O$	395.70	0.17
$(N)_i$	397.66	0.11
$(NO)_O$	398.10	0.12
$(NO_2)_O$	399.81	0.03
$(NO)_i$	399.85	0.10

so that the BE of N 1s for the $(N)_O$ species agrees with one of the experimental values, 395.7 eV [27]. The error of this evaluation is given roughly by the standard deviation of the Ti $2p_{3/2}$ levels within the unit cell, because the considered unit cell would not be large enough if the error is large.

We list in table 1 the N 1s binding energies calculated by the self-consistent core levels with errors estimated by the Ti $2p_{3/2}$ levels within the unit cell. The error is at most 0.2 eV, which is small enough to distinguish the N 1s binding energies among the N species. The $(NO)_i$ and $(NO_2)_O$ species are accompanied by a large distortion of the TiO_2 lattice, so we expect that these species may found mostly at the surface or in the voids of the solid, as suggested [22]. The $(N)_i$ and $(NO)_O$ can be interpreted as an intermediate state from weak bonding with an isolated molecule (BE = 400 eV) to an atomic N chemisorption with the lattice Ti (BE = 396 eV).

We examined the experimental XPS spectra of the samples prepared by different methods. A powder sample was obtained by treating anatase TiO_2 powder (ST01, Ishihara Sangyo Kaisha Ltd) in the NH_3 (67%)/Ar atmosphere for 3 h at 600 °C (denoted as Powder 1). We also prepared another powder sample (denoted as Powder 2) by hydrolysis of $TiCl_4$ with NH_4OH, followed by calcination at 400 °C, as reported by Sato [19]. The film sample was prepared by sputtering the TiO_2 target in N_2 (40%)/Ar gas mixture and with post-annealing at 550 °C in N_2 gas for 4 h (denoted as Film). These samples showed fairly good photocatalytic activity under visible light [1, 19].

In figure 3, we show the XPS spectra of Powder 1, Powder 2, and the film along with the BEs obtained by the FLAPW calculations. Powder 1 and the film samples show peaks at around 396 and 398 eV in addition to the peak at 400 eV, while only the peak at 400 eV is observed in Powder 2, suggesting that the N species in Powder 2 is different from that in Powder 1 or Film. In fact, the chemical stabilities among these samples are different; the photocatalytic activity under visible light for Powder 2 disappeared after the sample was heated in air at 500 °C, while Powder 1 still exhibited significant visible-light photocatalysis even after annealing in air at 550 °C [28]. These results indicate that the states with the lower BEs, namely 396 and 398 eV, are chemically more stable. The decomposed XPS peaks coincide very well with the calculated BEs. Besides the peak at 396 eV, which is assumed to be $(N)_O$, the peaks at 398 and 400 eV are assigned to be $(N)_i$ or $(NO)_O$ and $(NO)_i$ or $(NO_2)_O$, respectively. In Powder 2, $(NO_2)_O$ or $(NO)_i$ is suggested to dominate among the N species. This is considered to be a consequence of the hydrolysis process. In fact, detailed studies of the formation

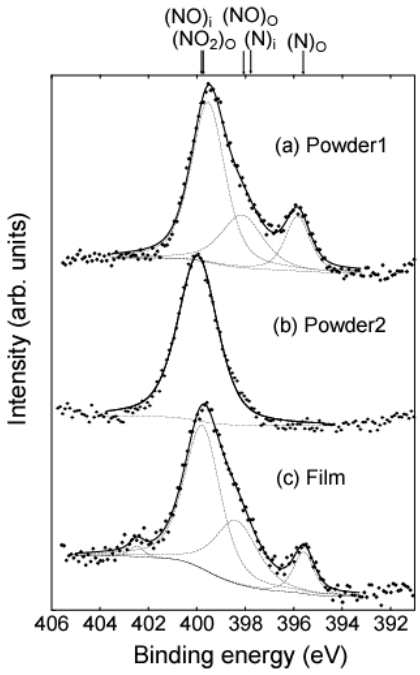

Figure 3. The measured x-ray photoemission spectra of the N 1s states for (a) Powder 1, (b) Powder 2, and (c) Film. The peak decompositions were performed to find the detailed peak positions. The binding energies evaluated by the FLAPW calculations (table 1) are indicated at the top.

energies show that $(NO_2)_O$ and $(NO)_i$ are stabilized in oxygen-rich conditions and, on going to the Ti-rich condition, $(N)_i$ and $(NO)_O$ and then $(N)_O$ become stable [29]. This explains why Powder 1, nitrified under rather reducing conditions, gives the peaks at 398 and 396 eV, and shows higher thermal stability than Powder 2. Note that the reducing condition may introduce oxygen defects. More efficient and less oxygen-defect nitrification can thus be realized by using an oxygen-containing nitrogen gas source such as NO [29].

We performed first-principles calculations for materials design of the visible-light sensitized photocatalyst as well as comprehensive studies regarding possible N complex species introduced in TiO_2. We also investigated the effects of different nitrification conditions. The substitutional N for oxygen is stable under a reduced process condition, while NO_x species may appear under an O-rich process condition. The calculated results show good agreement with the experimental XPS spectra and consistency with the trend in the process conditions. It is clear that realizing the N species in a more controlled way via the process conditions is crucial to achieving optimized photocatalytic performance.

The active wavelength of $TiO_{2-x}N_x$, of less than 500 nm, promises a wide range of applications. In fact, recently various kinds of products using this photocatalyst (V-CAT, Toyota Tsusho Co.), including wallpaper, cloth, coating for glasses, etc, have been commercialized. Their photocatalytic functions, such as anti-bacteria, deodorizing, and purifying the air, proved to be significant under interior lighting over conventional TiO_2.

4. Half-Heusler-type thermoelectric materials

Complex alloy systems have been of considerable interest in recent years for their intriguing transport properties, in particular aiming for thermoelectric applications along with increasing concern about environmental issue. The recently reported complex system, $AgPb_mSbTe_{2+m}$ ($m \sim 18$), showed a dimensionless thermoelectric figure of merit ZT ($=\sigma S^2/\kappa$, where σ is the electrical conductivity, S is the Seebeck coefficient, and κ is the thermal conductivity) as large as 2.2 at 800 K, which was the highest value ever reported in bulk systems [30]. Such a high value of ZT was realized by the possession of a large Seebeck coefficient $S = 380\ \mu V\ K^{-1}$ coupled with a low thermal conductivity $\kappa = 1.1\ W\ mK^{-1}$ at 800 K. An interesting structural feature was found in electron microscopy observations, suggesting the formation of Ag–Sb nanodots in the PbTe matrix. In fact, first-principles calculations implied that Ag and Sb ions tend to locate closer to make a pair-wise complex, which is consistent with the formation of Ag–Sb nanodots and the very low thermal conductivity [31]. Also, it was shown that a high Seebeck coefficient and electrical conductivity are maintained, thereby leading to the possession of a high ZT beyond that of PbTe. Despite such a high ZT, the inclusion of toxic elements such as Pb and Te may limit applications.

MNiSn-based (M = Ti, Zr, Hf) compounds are one of the most promising n-type thermoelectric materials, possibly consisting of no toxic elements [32]. These are often referred to as the half-Heusler compounds, possessing the cubic MgAgAs-type structure where half of the Ni atoms in the full-Heusler alloys MNi_2Sn are removed to form an ordered lattice of vacancies. Previous studies showed that they have a relatively narrow band gap of 0.1–0.5 eV as well as a high Seebeck coefficient and high electrical conductivity, thus yielding a large power factor (PF $= S^2\sigma$). One of the challenges was to reduce the thermal conductivity to increase ZT. For this purpose, several isoelectronic alloys with substitutions for M and Ni sites have been studied to introduce mass fluctuations and strain field effects [33, 34]. Another prescription is to change the carrier concentration, which is often realized by Sb doping for Sn in these n-type half-Heusler compounds, for maximizing PF and ZT [35]. Hohl *et al* reported $ZT = 0.5$ at 700 K in $(Zr_{0.5}Hf_{0.5})_{0.99}Ta_{0.01}NiSn$ [36], Shen *et al* reached a higher $ZT = 0.7$ at 800 K in $Hf_{0.5}Zr_{0.5}Ni_{0.8}Pd_{0.2}Sn_{0.99}Sb_{0.01}$ [37], and Kim *et al* reported a similar $ZT = 0.78$ at 770 K in $Ti_{0.95}Hf_{0.05}NiSn_{0.99}Sb_{0.01}$ [38]. Sakurada and Shutoh reported $ZT = 1.5$ at 700 K in $Ti_{0.5}Zr_{0.25}Hf_{0.25}NiSn_{0.998}Sb_{0.002}$ prepared by arc-melting and hot-press sintering [39], which is much higher than that in any previous reports. Their results showed significant effects on reducing thermal conductivity by double isoelectronic substitutions for the M site, i.e. the coexistence of Ti, Zr, and Hf. Recently, Culp *et al* evaluated ingot samples to have $ZT \sim 0.5$ at $T \sim 700$ K for $Ti_{0.5}Zr_{0.25}Hf_{0.25}NiSn_{0.99}Sb_{0.01}$ and a rather higher $ZT = 0.81$ at $T = 1025$ K for $Hf_{0.75}Zr_{0.25}NiSn_{0.975}Sb_{0.025}$ [40]. They found a large disagreement in thermal conductivity with that by Sakurada and Shutoh (6 W mK^{-1} versus 3 W mK^{-1}).

To realize high-performance bulk thermoelectrics, we have performed first-principles materials design for the MNiSn-based half-Heusler compounds. Inspired by the reported high thermoelectric properties in $AgPb_mSbTe_{2+m}$ ($m \sim 18$) [30, 31], we introduced pair-wise co-doping, i.e. A^+–B^- (where A^+ and B^+ are positively and negatively charged ions, respectively), which screens long-range Coulomb interaction with electrons but effectively plays a role as phonon scattering centers. We have thus considered the following requirements for designing high-performance thermoelectric materials: (i) a co-doping with simultaneous substitutions for two of three sites in the half-Heusler compound is introduced, but keeping the number of valences of 18 to ensure the semiconducting state; (ii) these two substitutional dopants energetically take a stable configuration, where they are located closer to each other in order to keep the charge neutrality in a nanoscale region around the dopants; and finally (iii) the predicted thermoelectric properties show an improvement over the system without co-doping.

We used PAW-VASP code for the first-principles calculations. The generalized gradient approximation was used for the exchange and correlation potential. To calculate doped systems and their formation energies, we used supercells sized from $Ti_4Ni_4Sn_4$ to $Ti_{32}Ni_{32}Sn_{32}$ with/without substitutional dopants. The formation energy ϕ_f for substitutional doping of A for a Ti site is calculated by $\phi_f[\mathrm{Ti} \to \mathrm{A}] = E(\mathrm{Ti}_{n-1}\mathrm{ANi}_n\mathrm{Sn}_n) - E(\mathrm{Ti}_n\mathrm{Ni}_n\mathrm{Sn}_n) - \mu(\mathrm{A}) + \mu(\mathrm{Ti})$, where E is the total energy of the system and μ is the chemical potential of the constituent element in its standard metallic state. Similarly, we evaluated the formation energy for co-doping, taking the standard metallic state of each element as the reference. The lower formation energy for the dopant means that it is more stable in the crystal. We only consider a solid solution with doping, which is ensured for a small doping level as performed in experiment shown below. We used sampling **k** points of $3 \times 3 \times 3$, and the stable structure was assumed when the atomic force was less than 0.02 eV $Å^{-1}$. To calculate band structures and transport properties, we employed the FLAPW method. The electrical conductivity σ and the Seebeck coefficient S were calculated by using the Bloch–Boltzmann expressions:

$$\sigma_E(\varepsilon, T) = e^2 N(\varepsilon) \upsilon^2(\varepsilon) \tau(\varepsilon, T), \tag{1}$$

$$\sigma(T) = \int \sigma_E(\varepsilon, T) \left[-\frac{\partial f(\varepsilon)}{\partial \varepsilon} \right] d\varepsilon, \tag{2}$$

$$S(T) = \frac{1}{eT\sigma(T)} \int (\varepsilon - \mu) \sigma_E(\varepsilon, T) \left[-\frac{\partial f(\varepsilon)}{\partial \varepsilon} \right] d\varepsilon, \tag{3}$$

where N denotes the density of states, υ the group velocity, f the Fermi function, and μ the chemical potential. In these expressions, we neglected the energy dependence of the relaxation time τ. Then S can be determined unambiguously by first-principles calculations. This approximation has worked well for many thermoelectric materials, as shown in the previous works [41–43]. It is still difficult to evaluate the electrical conductivity because of τ, which involves complicated scattering processes. In this work, we roughly

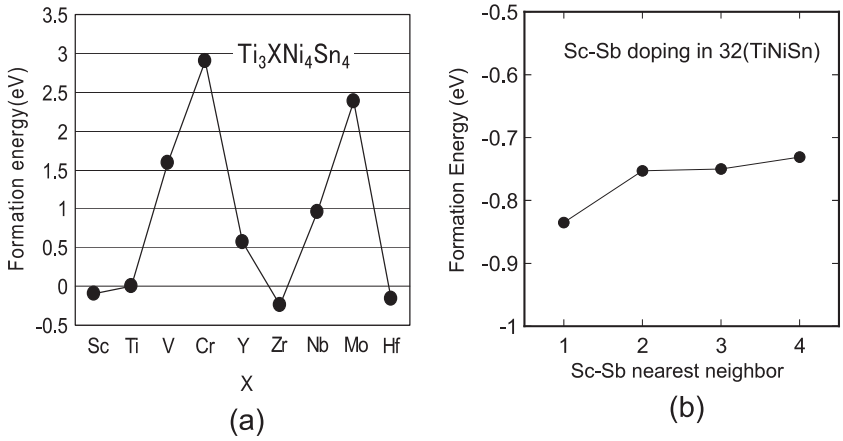

Figure 4. (a) Calculated formation energies of each substitutional doping for a Ti site in $Ti_4Ni_4Sn_4$. (b) Calculated formation energies with different configurations of Sc and Sb atoms in the $Ti_{32}Ni_{32}Sn_{32}$ supercell.

estimate a relative value of electrical conductivity with respect to the non-doped material, σ/σ_0, assuming that τ is constant.

The formation energies of each single dopant for a Ti site in $Ti_4Ni_4Sn_4$ are shown in figure 4(a). Elements such as Sc(−1), Y(−1), Zr, and Hf are chosen as possible dopants in the Ti site. Similarly, we obtained stable substitutional dopants Co(−1), Rh(−1), Pd, and Pt for the Ni site, and Si, Ge, and Sb(+1) for the Sn site. Here (+1) or (−1) means possible electron or hole doping, respectively. From these results we took possible combinations of the pair-wise co-doping and evaluated the formation energies and thermoelectric properties, as listed in table 2. The other co-dopings such as RhSb were not as stable as those in table 2. Note that, although the only Y doping gave a positive formation energy, co-doping with Sb showed a negative formation energy. Compared to the undoped system, we found an improvement in S by Y–Sb or Sc–Sb co-doping, while σ remains similar to that of the undoped system, thus we expected a larger PF. On the other hand, the Co–Sb co-doped system shows lower thermoelectric properties. We also calculated the formation energies with different configurations of Sc and Sb atoms in the $Ti_{32}Ni_{32}Sn_{32}$ supercell, as shown in figure 4(b). From these results, we found that the stable configuration of Sc and Sb is the nearest-neighboring configuration. Therefore the Sc–Sb (and also Y–Sb) co-doping ensures local charge neutrality, so that effective long-range Coulomb interaction with conduction electrons around the dopants dies off. A similar situation was found in AgSb-doped PbTe [31]. Finally, we concluded that co-doping of Y–Sb or Sc–Sb is most suitable for enhancement of the thermoelectric properties.

We applied the present materials design to the compound $(Ti_{0.5}Zr_{0.25}Hf_{0.25})NiSn$. Partial substitution of Zr and Hf for Ti reduces the thermal conductivity and thereby elevates the ZT value [39]. These substitutions, however, may induce secondary phases and non-uniformities of the composition. Therefore we used the liquid quench (LQ) process after high-frequency induction (RF) melting [2]. SPS sintering was then employed to produce sintered compacts. The LQ process was indeed crucial for improving the uniformity of the half-Heusler phase, as observed in the x-ray diffraction and scanning electron microscopy results [3]. We prepared undoped $(Ti_{0.5}Zr_{0.25}Hf_{0.25})NiSn$ compound, Sb-doped compound, and Y–Sb co-doped compound. The doping concentration for the latter two systems was optimized so that the figure of merit ZT showed a maximum, i.e. 3%-Sb and 1%-YSb, respectively. The results are shown in figure 5. Improving the compositional homogeneity enhances ZT. Further significant enhancement of the thermoelectric performance by Y–Sb doping is observed, reaching $ZT = 0.96$ at 773 K. Note that the co-doped system was superior to the single Sb-doped system. Therefore an effect of Y–Sb co-doping is not just the result of optimization in the carrier concentration. A detailed structural analysis is currently being undertaken; three-dimensional (3D) atomic distributions obtained by the atomic probe technique show a one-dimensional chain feature of Y [3]. Therefore, nanostructural modification in such a co-doped system may be the key to enhancement of the thermoelectric properties.

Table 2. Calculated formation energies (F.E.) and thermoelectric properties (S, σ, and $PF = \sigma S^2$) for pair-wise co-doped systems, compared with those of the undoped system (denoted as S_0, σ_0 and $PF_0 = \sigma_0 S_0^2$). The thermoelectric properties were evaluated for a carrier concentration of 1.9×10^{20} cm^{-3} and a temperature of 600 K.

	F.E. (eV)	S (μV K^{-1})	σ/σ_0	PF/PF_0
Non-doped	0	−173.48	1	1
CoSb	−0.44	−165.77	0.83	0.76
ScSb	−0.93	−184.66	0.99	1.12
YSb	−0.37	−183.18	1.03	1.15

5. Conclusions

Through the development of visible-light sensitized photocatalysts and high-performance thermoelectric materials, we have in particular emphasized materials design on the atomic scale using computation. The universality and applicability of these methods provide exciting insight into many applications, and even lead to serendipity for new discoveries. Since density

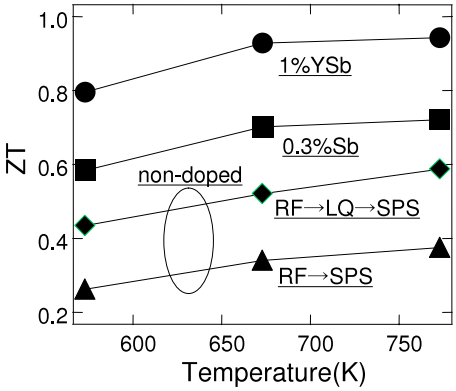

Figure 5. Experimentally evaluated thermoelectric figures of merit for undoped $(Ti_{0.5}Zr_{0.25}Hf_{0.25})NiSn$ compound, Sb-doped compound, and Y–Sb co-doped compound. We employed the liquid quench (LQ) process between high-frequency induction (RF) melting and SPS sintering, resulting in improved compositional homogeneity and *ZT*, as shown clearly for the undoped samples.

functional theory was developed in 1964, first-principles calculation has now become a practical tool in materials research, even in industry. The essentials for success will be close collaboration between theory and experiment, the pursuit of meaningful models, and understanding the limitations and efficiency of both theory and experiment.

Acknowledgments

We are pleased to acknowledge and thank T Ohwaki, K Suzuki, Y Taga, H Kaga, T Tani, S Yamamoto, M Suzuki, N Takahashi, and U Mizutani for fruitful discussion and collaboration. We also thank E Wimmer, P Saxe, and A J Freeman for helpful discussion and computational support.

References

[1] Asahi R, Morikawa T, Ohwaki T, Aoki K and Taga Y 2001 *Science* **293** 269
[2] Hazama H, Asahi R, Matsubara M, Kaga H and Mizutani U 2006 *Proc. Ann. Mtg of TSJ (Fujisawa, JP, Aug.)* p 16
[3] Matsubara M, Asahi R, Nakagaki T, Isheim D and Seidman D N 2007 *Proc. 26th Int. Conf. Thermoelectrics (Jeju Island, June)* at press
[4] Saito T, Furuta T, Hwang J H, Kuramoto S, Nishino K, Suzuki N, Chen R, Yamada A, Ito K, Seno Y, Nonaka T, Ikehata H, Ngakasako N, Iwamoto C, Ikuhara Y and Sakuma T 2003 *Science* **300** 464
[5] Hafner J, Wolverton C and Ceder G 2006 *MRS Bull.* **31** 659
[6] Fujishima A and Honda K 1972 *Nature* **238** 37
[7] Ollis D F and Al-Ekabi H (ed) 1993 *Photocatalytic Purification and Treatment of Water and Air* (Amsterdam: Elsevier)
[8] Ghosh A K and Maruska H P 1977 *J. Electrochem. Soc.* **124** 1516
[9] Choi W, Termin A and Hoffmann M R 1994 *J. Phys. Chem.* **98** 13669
[10] Anpo M 1997 *Catal. Surv. Japan.* **1** 169
[11] Breckenridge R G and Hosler W R 1953 *Phys. Rev.* **91** 793
[12] Cronemeyer D C 1959 *Phys. Rev.* **113** 1222
[13] Sakata T and Kawai T 1983 *Energy Resources Through Photochemistry and Catalysis* ed M Grätzel (New York: Academic) pp 332–58
[14] Shockley W and Read W T Jr 1952 *Phys. Rev.* **87** 835
[15] Wimmer E, Krakauer H, Weinert M and Freeman A J 1981 *Phys. Rev.* B **24** 864
[16] Jansen H J F and Freeman A J 1984 *Phys. Rev.* B **30** 561
[17] Hedin L and Lundqvist B I 1971 *J. Phys. C: Solid State Phys.* **4** 2064
[18] Asahi R, Taga Y, Mannstadt W and Freeman A J 2000 *Phys. Rev.* B **61** 7459
[19] Sato S 1986 *Chem. Phys. Lett.* **123** 126
[20] Diwald O, Thompson T L, Zubkov T, Goralski E G, Walck S D and Yates J T Jr 2004 *J. Phys. Chem.* B **108** 6004
[21] Chen X and Burda C 2004 *J. Phys. Chem.* B **108** 15446
[22] Livraghi S, Votta A, Paganini M C and Giamello E 2005 *Chem. Commun.* 498
[23] Blochl P E 1994 *Phys. Rev.* B **50** 17953
[24] Kresse G and Furthmuller J 1996 *Comput. Mater. Sci.* **6** 15
[25] Kresse G and Furthmuller J 1996 *Phys. Rev.* B **54** 11169
[26] Perdew J P, Burke K and Ernzerhof M 1996 *Phys. Rev. Lett.* **77** 3865
[27] Saha N C and Tompkins H G 1992 *J. Appl. Phys.* **72** 3072
[28] Asahi R, Morikawa T, Ohwaki T, Aoki K and Taga Y 2002 *Science* **295** 627
[29] Asahi R and Morikawa T 2007 *Chem. Phys.* **339** 57
[30] Hsu K F, Loo S, Guo F, Chen W, Dyck J S, Uher C, Hogan T, Polychroniadis E K and Kanatzidis M G 2004 *Science* **303** 818
[31] Hazama H, Mizutani U and Asahi R 2006 *Phys. Rev.* B **73** 115108
[32] Poon S J 2001 *Semiconductors and Semimetals* vol 70, ed T M Tritt (New York: Academic) p 37
[33] Shen Q, Chen L, Goto T, Hirai T, Yang J, Meisner G P and Uher C 2001 *Appl. Phys. Lett.* **79** 4165
[34] Yang J, Meisner G P and Chen L 2004 *Appl. Phys. Lett.* **85** 1140
[35] Uher C, Yang J, Hu S, Morelli D T and Meisner G P 1999 *Phys. Rev.* B **59** 8615
[36] Hohl H, Ramirez A P, Goldmann C, Ernst G, Wolfing B and Bucher E 1999 *J. Phys.: Condens. Matter* **11** 1697
[37] Shen Q, Chen L, Goto T, Hirai T, Yang J, Meisner G P and Uher C 2001 *Appl. Phys. Lett.* **79** 4165
[38] Kim S W, Kimura Y and Mishima Y 2007 *Intermetallics* **15** 349
[39] Sakurada S and Shutoh N 2005 *Appl. Phys. Lett.* **86** 082105
[40] Culp S R, Poon S J, Hickman N, Tritt T M and Blumm J 2006 *Appl. Phys. Lett.* **88** 042106
[41] Nunes R W, Mazin I I and Singh D J 1999 *Phys. Rev.* B **59** 7969
[42] Kim S G, Mazin I I and Singh D J 1998 *Phys. Rev.* B **57** 619
[43] Singh D J and Mazin I I 1997 *Phys. Rev.* B **56** R1650